Physical Characteristics Controlling Radiation from Heterogeneous Ruptures—Finite Faults

Igor A. Beresnev[*1]

ABSTRACT

Kinematic simulations of ground motion require representations of the earthquake source: the distribution of final slip, parameters of the source time function, and the velocity of rupture travel. There is a significant ambiguity in prescribing these physical characteristics, causing uncertainty in the resulting motions that needs to be quantified. The representation integral is an appropriate tool: it allows exact calculation of the source effect in both the near and far fields in the frequency band of practical interest. The commonly used distributions of slip have a k-square shape of their wavenumber spectra. Various k-square slips change the slope of the radiated spectra in the range of ~-2.5 and -4.0 in both the far and near fields. The spectra generated by randomly disturbed constant slip are indistinguishable from those emitted by k-square faults. In both cases, variations in peak values of ground velocity and acceleration between realizations are relatively insignificant: under $\sim15\%$ for the same hypocenter position. The slopes of the Fourier spectra produced exclusively by the form of the slip function and the slip heterogeneity are equivalent to using a formal kappa filter with κ ranging from ~0.025 to 0.045 s. No ad hoc high-frequency filtering (of kappa or f_{max} type) is required if fault finiteness is accounted for. Geometric irregularity of rupture fronts, at least for the way the front progression is randomized in our case, does not appreciably affect the slopes of the spectra. Its principal effect is in blurring the directivity, reducing the sharpness of radiated pulses. The most influential parameter affecting the peak ground motions for several commonly used slip functions is the maximum velocity of slip: scaling of v_{max} causes a proportional scaling in peak ground acceleration. This parameter is the most important to constrain to reduce ambiguities in predicted ground motions.

KEY POINTS

- What are the variations in ground motions and their spectra due to heterogeneities in rupture characteristics?
- Different realizations of heterogeneous ruptures produce the effect equivalent to a variable kappa operator.
- Diverse scenarios on finite faults can explain the variations in the high-frequency behavior of radiated spectra.

INTRODUCTION

Simulation of radiation from large earthquakes via kinematic models is an important tool in quantitative assessment of seismic hazards (Beresnev and Atkinson, 2002; Aagaard and Heaton, 2004; Aagaard et al., 2008; Graves et al., 2008; Schmedes and Archuleta, 2008; Aagaard, Graves, Rodgers, et al., 2010; Aagaard, Graves, Schwartz, et al., 2010; Graves and Pitarka, 2010, 2016; Ruiz et al., 2011; Skarlatoudis et al., 2015; Rodgers et al., 2019, 2020; Infantino et al., 2020; Lee et al., 2020; Fayjaloun et al., 2021; Razafindrakoto et al., 2021; Pitarka, Akinci, et al., 2022; Pitarka, Graves, et al., 2022). Models of this type have been adopted as the Broadband Platform (BBP) for ground-motion

simulation by the Southern California Earthquake Center (SCEC) (now Statewide California Earthquake Center) (Dreger and Jordan, 2015). In the kinematic approach, a rupture model has to be prescribed. The input variables include: the distribution of static (final) slip on the fault, the temporal shape of slip (the source time function), and the velocity of rupture propagation. However, the details of all these quantities, as functions of the position on the fault, are not well constrained by the source-inversion studies, allowing a significant leeway in formulating the specific concepts. The published inversions carry significant and often unknown uncertainties and trade-offs; their veracity in many cases cannot be ascertained with confidence (Beresnev, 2003, 2013, 2023b).

Because of the fundamental lack of knowledge, alternative descriptions of the source process coexist, each considered to

1. Department of the Earth, Atmosphere, and Climate, Iowa State University, Ames, Iowa, U.S.A., https://orcid.org/0000-0002-4050-919X (IAB)

*Corresponding author: beresnev@iastate.edu

be equally plausible (see the following for specific examples of choices). The range of the available input models causes the uncertainty of the modeling type in the forecasted ground motions: it needs to be systematically and rigorously quantified in the entire frequency band of engineering significance up to ~50 Hz. Such a quantification remains an open task. Identifying the characteristics of faulting that are most important in controlling the radiation will help focus future observational efforts on better constraining these specific crucial parameters.

In the state-of-the-art approach, known as hybrid, as summarized by Graves and Pitarka (2010), low seismic frequencies are calculated deterministically while higher ones (greater than ~1 Hz) are calculated stochastically. The hybrid technique is the basis of the SCEC BBP. However, the stochastic approach to the simulation of high-frequency content is inaccurate, and its limitations must be realized. Its key features include the subdivision of the fault plane into subfaults and the representation of each as a point-source radiator of an omega-square spectrum with random phasing. Contributions from all subfaults are summed to compute the fault's radiation. Such a representation is oversimplified. The field from a single point source is an asymptotic expression only valid at wavelengths much exceeding the fault dimensions. It lacks the effects of geometric interference and the near-field radiation terms playing a key role close to finite earthquake sources. The summation of randomly disturbed point-source radiation does not correctly capture the near-fault effects that are important near large earthquakes.

The stochastic simulations are also known to suffer from the dependence on the subjective choice of the subfault size (Beresnev and Atkinson, 2002). First, this approach replaces the continuous integration over the fault plane with discrete summation. Second, judgment needs to be made regarding the assignment of a corner frequency to a subsource based on its size (Beresnev and Atkinson, 1997, their equation 14; Graves and Pitarka, 2010, their equation 13). Such an association is nonunique. On the other hand, the corner frequency is a controlling parameter of the resulting radiation spectrum. The ambiguity that follows is one of the most severe weaknesses of stochastic modeling. Most studies make virtually arbitrary decisions about the subfault size without explicitly addressing such dependence. Using the stochastic method to investigate the relative effect of the important characteristics of faulting, such as the slip distribution, temporal slip function, or rupture velocity, on seismic radiation may lead to erroneous conclusions.

In the quantitative assessment of the role of different characteristics of faulting in forming the radiation, the representation integral of elasticity is a powerful analytical tool. Its key advantage is that, within the realm of applicability, it represents the exact seismic field, valid at any frequency and fully accounting for near-field phenomena. The representation integral allows the isolation of the pure source effect in a rigorous mathematical manner. We will use it to quantitatively evaluate the relative significance of the various distributions of static slip, parameters of the source time function, and irregular rupture fronts in forming earthquake radiation.

THE SIMULATION METHOD

Our simulations are based on the numerical evaluation of the full representation integral of elasticity for a fault embedded in an elastic space (Aki and Richards, 1980, their equation 14.37; Beresnev, 2017b, his equation 1). The numerical procedure is fully described and validated by Beresnev (2017b), to which the reader is referred for brevity. The adopted space geometry allows us to focus on the pure source effect.

The fault is the right-lateral strike-slip. For the near-field calculations, the observation point is placed at 200 m above the upper corner of the fault and offset by 200 m in the direction x_2 perpendicular to the fault plane, thus having the coordinates $\mathbf{x} = \{0, 200, 200\}$ m as shown in Beresnev (2017a, his fig. 1). To compare with known asymptotic cases, we will also consider an observation point in the far field to be subsequently specified. The integral is computed for the fault-normal component of the radiated displacement as typically the larger component being of primary interest to structural-response analyses (Bray and Rodriguez-Marek, 2004; Beresnev, 2022c), which is subsequently low-pass filtered at 45 Hz (Beresnev, 2017b). The traces of ground velocity and acceleration are obtained by numerical differentiation of the displacement seismogram. As detailed by Beresnev (2017b), differentiation acts to significantly enhance numerical noise, mandating a high precision in the evaluation of the integral. Accordingly, unless otherwise stated, all displacement time histories are calculated to the precision of six decimal places. The need to maintain high precision imposes practical limitations on the size of the fault that can be realistically analyzed in the near field. In the latter, for a sufficiently heterogeneous slip distribution in the integrand, numerical integration stops converging to the required precision already for fault dimensions approximately corresponding to an M 5 earthquake. For that reason, all the near-field calculations are performed for a 1200 × 1200 m fault corresponding to an M_w 4 earthquake, according to the empirical relationship between the rupture area and moment magnitude of Wells and Coppersmith (1994, their table 2A). The average offset $U = 0.035$ m in this case was calculated as $U = M_0/(\mu A)$, in which the moment M_0 was obtained from the moment magnitude and the fault area A from the equation of Wells and Coppersmith. Asymptotic far-field calculations do not suffer from the lack of convergence; accordingly, they will be performed for an M 5 fault with the respective $U = 0.14$ m. The fault dimensions corresponding to the asymptotic case will be introduced together with the discussion of the model. The shear modulus μ is calculated as $\mu = \beta^2 \rho$, in which the density ρ was taken as 2700 kg/m³,

and the shear-wave velocity β was obtained from the P-wave velocity of 5000 m/s as $\beta = 5000/\sqrt{3}$ m/s. Except when specifically noted, the rupture speed v is set to the constant value of 0.8β.

We adopt the source time function that radiates the omega-square Fourier spectrum into the far field (Beresnev and Atkinson, 1997, their equation 6). The slip-velocity function (first derivative of slip) is

$$\Delta \dot{u}(\boldsymbol{\xi},t) = U(\boldsymbol{\xi})\frac{t}{\tau^2}e^{-t/\tau} \equiv U(\boldsymbol{\xi})\Delta \dot{u}_s(\boldsymbol{\xi},t), \tag{1}$$

$$\tau = \frac{U(\boldsymbol{\xi})}{ev_{\max}(\boldsymbol{\xi})}, \tag{2}$$

in which $\boldsymbol{\xi} = \{\xi_1,\xi_3\}$ is the position on the fault surface, and $v_{\max}$ is the peak (maximum) velocity of slip. For convenience, we have introduced a temporal shape function $\Delta \dot{u}_s(\boldsymbol{\xi},t)$, to isolate it from the static slip $U(\boldsymbol{\xi})$. The corner frequency of the radiated omega-square spectrum is the inverse of τ: $\omega_c = 1/\tau$ (Beresnev, 2001, his equation 3). The slip is controlled by two fundamental physical parameters: U and $v_{\max}$, the former defining the low-frequency asymptotic plateau of the radiated spectrum in the far field and the latter the strength of high-frequency radiation. Their combination determines the rise time τ_r at a point on the fault in both the general omega-n and dynamically compatible slip functions (Beresnev, 2022a, his equations 12 and 13). The quantity τ_r, therefore, is not an independent rupture parameter. For example, the rise time for the omega-square model in equations (1) and (2) is $\tau_r = 2.44\,U/v_{\max}$ (Beresnev, 2022a, his equation 13). The equations also show that, in the omega-square slip-velocity function, the effect of static slip U cannot be separated from the effect of the shape function $\Delta \dot{u}_s$, the latter also depending on U. According to equations (1) and (2), the source time function and the corner frequency are generally variable over the fault plane.

Guatteri et al. (2004, their figs. 3 and 4) summarized and parameterized the functional forms of slip-rate functions produced from a large number of dynamic simulations (for brevity, the article by Guatteri et al., 2004 will subsequently be cited without the year as Guatteri et al.). They established that the shapes varied in the width of the main pulse and the height of the long tail. Dynamic simulations conducted by Pitarka, Graves, et al. (2022, their fig. 6) reproduced a similar range of patterns. Beresnev (2022a) identified the end-member cases of the Guatteri et al. shapes as those having a "short pulse, high tail" and a "wide pulse, low tail" configurations. He found that these limiting cases are equivalent to the omega-n functions with n ranging from ~1.5 to 3.5 ($n = 2$ corresponding to the omega-square case). Other studies have proposed similar dynamically compatible analytical generalizations for kinematic modeling (e.g., Tinti et al., 2005; Liu et al., 2006). All these formulations are approximately equivalent (Graves and Pitarka, 2010, their fig. 3).

The radiated Fourier spectra of the ith component of seismic displacement are computed from the analytical Fourier transform of the representation integral (Beresnev, 2017a, his equations 4 and 5),

$$u_i(\mathbf{x},\omega) = \frac{\mu}{4\pi\rho}\int\int \Delta u(\boldsymbol{\xi},\omega)e^{-i\omega\Delta t(\boldsymbol{\xi})}$$
$$\left[\frac{30\gamma_i n_p \gamma_p \gamma_q v_q - 6v_i n_p \gamma_p - 6n_i \gamma_q v_q}{R^4}t_1(\omega)\right.$$
$$+\frac{12\gamma_i n_p \gamma_p \gamma_q v_q - 2v_i n_p \gamma_p - 2n_i \gamma_q v_q}{\alpha^2 R^2}e^{-i\omega\frac{R}{\alpha}}$$
$$-\frac{12\gamma_i n_p \gamma_p \gamma_q v_q - 3v_i n_p \gamma_p - 3n_i \gamma_q v_q}{\beta^2 R^2}e^{-i\omega\frac{R}{\beta}}+\frac{2\gamma_i n_p \gamma_p \gamma_q v_q}{\alpha^3 R}i\omega e^{-i\omega\frac{R}{\alpha}}$$
$$\left.-\frac{2\gamma_i n_p \gamma_p \gamma_q v_q - v_i n_p \gamma_p - n_i \gamma_q v_q}{\beta^3 R}i\omega e^{-i\omega\frac{R}{\beta}}\right]d\Sigma(\boldsymbol{\xi}), \tag{3}$$

$$t_1(\omega) = \frac{1}{\omega}\left[e^{-i\omega\frac{R}{\beta}}\left(i\frac{R}{\beta}+\frac{1}{\omega}\right) - e^{-i\omega\frac{R}{\alpha}}\left(i\frac{R}{\alpha}+\frac{1}{\omega}\right)\right]. \tag{4}$$

Here, $\Delta u(\boldsymbol{\xi},\omega) = U(\boldsymbol{\xi})/[i\omega(1 + i\omega\tau)^2]$ is the complex spectrum of the omega-square source time function; $\mathbf{n}$ is the unit vector in the direction of slip; v is the unit normal to the fault; $R = |\mathbf{x} - \boldsymbol{\xi}|$, $\gamma = (\mathbf{x} - \boldsymbol{\xi})/R$, and α is the P-wave speed. The double integration is over the fault plane $\Sigma(\boldsymbol{\xi})$. For the strike-slip fault under consideration, all geometric coefficients $\gamma_i n_p \gamma_p \gamma_q v_q$, $v_i n_p \gamma_p$, and $n_i \gamma_q v_q$ in the integrand reduce to simple analytical forms (Beresnev, 2017b, his equations 7; Beresnev, 2021, his equations 2). Unless otherwise noted, the spectra are calculated to the precision of three decimal places.

Compared to Beresnev (2017a), equation (3) has been written in the general way to (1) allow $\Delta u(\boldsymbol{\xi},\omega)$ to be fault-position dependent and (2) replace the time delay r/v due to radial rupture propagation with constant speed to distance r from the hypocenter with the general fault-position-dependent delay $\Delta t(\boldsymbol{\xi})$. Hence, $\Delta u(\boldsymbol{\xi},\omega)$ is now in the integrand, and the phase-delay exponential multiplier in the integrand has changed from $\exp(-i\omega r/v)$ to the general $exp[-i\omega\Delta t(\boldsymbol{\xi})]$ (Beresnev and Roxby, 2021).

SLIP-DISTRIBUTION MODELS
k^{-2} model
There is a significant uncertainty in prescribing the spatial distribution of fault slip for future earthquakes: the models have ranged from uniform to purely random (Aagaard and Heaton, 2004). A popular slip distribution has the functional form spatial spectrum for which decays as k^{-2}, in which k is the wavenumber. The k-square model has often been used in the synthetic rupture-slip generators for seismic hazard computations (Herrero and Bernard, 1994; Somerville et al., 1999, pp. 75–76; Mai and Beroza, 2002; Graves and Pitarka, 2010, p. 2096; Schmedes et al., 2013, p. 1121; Infantino et al., 2020, pp. 2563–2564; Rodgers et al., 2020, p. 2866).

A useful asymptotic model illustrating the possible effects of slip distribution on the spectrum of shear-wave radiation from finite faults is the approximation of the far field of a small line source with unidirectional rupture moving with constant speed,

$$u_i(\mathbf{x},\omega) = \text{const} \, \Delta \dot{u}_s(\omega) U \left[\omega \left(\frac{\cos \Psi}{\beta} - \frac{1}{v} \right) \right], \qquad (5)$$

in which const is a dimensional constant collapsed here for brevity, and Ψ is the angle between the direction to the receiver and the fault line (Beresnev, 2022b, his equation 9). Here, $U(k)$ is the 1D spatial Fourier transform of the slip distribution along the fault line, taken at the wavenumber $k = \omega(\cos \Psi/\beta - 1/v)$, and $\Delta \dot{u}_s(\omega)$ is the frequency spectrum of the shape function. In this approximation, this spectrum is assumed to be independent of the position on the fault, allowing one to take it out of the integral in equation (3). A subset of such models is, for example, the radiated spectrum of Herrero and Bernard (1994, their equation 24, also reproduced in their abstract; Beresnev, 2022b). Because the position dependence of $\Delta \dot{u}_s(\xi,t)$ is through the quantity τ (the inverse of the corner frequency), the latter in equation (5) is assumed to be constant over the fault. It is a particular case of the general behavior in equation (2). Equation (5) illustrates that the Fourier frequency spectrum of the far-field displacement is the frequency spectrum of the slip-rate function multiplied by the spatial spectrum of slip. In the following, equation (5) will be used to provide comparative insight into the results of the accurate numerical modeling with spatially variable $\tau(\xi)$ having no similar restrictions.

We adopt the general k-square spectral model in the form

$$|U(k_1,k_3)| = \frac{ULW}{\sqrt{1 + (k_1 L)^2 + (k_3 W)^2}}, \qquad (6)$$

in which $|U(k_1,k_3)|$ is the 2D amplitude spatial spectrum of slip over the fault (the Fourier transform is recognized by its arguments); U is the average slip; and L and W are the fault length and width (Somerville *et al.*, 1999, p. 75; Gallovič and Brokešová, 2004, their equation 6). The phase in the spectrum is randomly drawn from the uniform distribution between $-\pi$ and π, as done by Graves and Pitarka (2010, their equation A3). In the case of the square 1200×1200 m fault, two spatial-discretization intervals $\Delta \xi$ were investigated, which will be arbitrarily termed the "coarse"- and "fine"-resolution models: $\Delta \xi = L/99$ ($N = 100$ samples along both length and width) and $\Delta \xi = L/199$ (200 samples). This gives the respective values of $\Delta \xi = 12$ and 6 m. The corresponding sampling interval in the spatial-frequency domain in the discrete Fourier transform is $\Delta s = 1/(N\Delta \xi)$, and wavenumber sampling is $\Delta k = 2\pi \Delta s$. The discrete values of the complex spectrum at k from zero to the Nyquist wavenumber $2\pi[1/(2\Delta \xi)]$ spaced at Δk were produced in each direction k_1 and k_3 from

equation (6) with the random phase. The resulting spatial grid of spectral values was inverted via the inverse spatial Fourier transform to obtain $U(\xi_1,\xi_3)$, for which real part was taken. If the minimum of the resulting slip distribution was less than zero, it was subtracted from all the values to eliminate negative slip. Also in that case, to avoid the slip on certain parts to be exactly zero, a small number, equal to one-hundredth of the modulus of the minimum, was added to the distribution. The grid $U(\xi_1,\xi_3)$ was then renormalized by multiplying it by $U/\overline{U}(\xi_1,\xi_3)$, in which $\overline{U}(\xi_1,\xi_3)$ is the average, to offset the scaling introduced by the discrete Fourier transform and ensure the correct value of the average slip U for the target earthquake. The grid was then interpolated with a third-order polynomial to obtain a smooth function $U(\xi_1,\xi_3)$ for the numerical integration.

Randomized model

Similarly to Beresnev (2017a), we will also analyze radiation from a randomized slip distribution. In this case, the distribution is generated by superimposing a random component on constant U to produce $U(\xi_1,\xi_3) = U[1 + \eta(\xi_1,\xi_3)]$ in which the variable $\eta(\xi_1,\xi_3)$ is drawn from a normal distribution with zero mean and standard deviation of 0.3, constrained to equal -1 if its value accidentally fell below it. The latter modification to the k^{-2} model was introduced to avoid an exactly zero slip. Because -1 exceeds three standard deviations, such a value was highly unlikely; that is why no further adjustments were made. Unless otherwise noted, this distribution was generated on a grid with a step of $L/20$ in each direction ξ_1 and ξ_3 and then interpolated with a third-order polynomial to a smooth $U(\xi_1,\xi_3)$.

EFFECT OF DISTRIBUTION OF STATIC SLIP

Investigations exist that have addressed the effect of different realizations of slip on the resulting ground motions (e.g., Aagaard, Graves, Rodgers, *et al.*, 2010; Infantino *et al.*, 2020). The frequencies greater than 1 Hz were simulated approximately through the stochastic method by Aagaard, Graves, Rodgers, *et al.* (2010) and via training of artificial neural networks by Infantino *et al.* (2020). What is lacking is a comprehensive rigorous study isolating the theoretical source effect in the entire frequency band, including the near field. The representation integral is the appropriate tool for this task.

k^{-2} model

Far field of a narrow unidirectional rupture. We begin with the analysis of an asymptotic case of far-field radiation from a unidirectional rupture moving with constant speed on a small narrow fault (the Haskell model), for which analytical solutions are available (e.g., Aki and Richards, 1980, their equation 14.18). The solution for the shape function $\Delta \dot{u}_s(t)$ that is the same on the entire fault is given by equation (5). Because our adopted slip-rate spectrum has the omega-square

shape, and if the slip spectrum $U(k)$ also exhibits the k-square decay, then the multiplication in equation (5) leads to the ω^{-4} fall-off in the radiated frequency spectrum.

Beresnev (2022b, his equation 19) generalized equation (5) to a more realistic, but still 1D, case of $\Delta\dot{u}_s(\xi,t)$ depending on both ξ and t. We wish to complement this earlier analysis with the exact calculations from the full integral in equation (3), only restricted by setting the distance to the observation point within the validity of the far-field condition. As noted earlier, this case will be analyzed for a fault corresponding to a M 5 earthquake. The length L = 3400 m, approximately corresponding to this magnitude, is again calculated from the Wells–Coppersmith relationship. The spatial-discretization interval in both directions is still taken as $\Delta\xi = L/99$; the narrow-width condition is followed by setting $W = 5\Delta\xi$. There are $N_1 = 100$ samples along the length and $N_3 = 6$ samples along the width. The Nyquist wavenumber did not change; N_1 and N_3 discrete values of the complex wavenumber spectrum were then produced for k_1 and k_3 from equation (6) with random phase to be inverted for the k-square 2D slip distribution along the narrow plane.

The most restrictive condition on the distance to the observation point leading to the small-source approximation is

$$r_0 \gg \frac{2L^2}{\lambda},\tag{7}$$

in which λ is the wavelength (Aki and Richards, 1980, their equation 14.12). Using L = 3400 m and $\lambda = (\beta/50)$ m (at the frequency of 50 Hz), we obtain the limits of applicability of the approximation as $r_0 \gg 400$ km. Accordingly, the coordinates of the observation point in this calculation are arbitrarily set to $\{10^4, 0, 0\}$ km. Such distances do not represent practical interest but do provide a useful insight. The specific distance value does not carry particular significance; it appears as a multiplier in the constant term in equation (5) and in this approximation it merely serves as a scaling factor. The hypocenter is in the middle of the vertical edge of the fault opposite to the observation point with the coordinates of $\{0, 0, -W/2\}$ m. The rupture propagation is thus unilateral toward the observation station. Until otherwise noted in the discussion of the irregular rupture fronts, the rupture propagation is radial from the hypocenter with concentric fronts, although the fronts are nearly straight on the narrow fault. The time delay is thus $\Delta t(\xi) = r/v$, in which v is constant.

In this calculation, the slip-velocity function $\Delta\dot{u}_s(\xi,t)$ is variable over the fault. This is achieved through the use of equation (2) to calculate the variable corner frequency (the inverse of τ). In equation (2), v_{max} will be set to a constant representative value of 1 m/s. In doing so, we do not loose generality because τ still varies in proportion to the k-square distribution $U(\xi)$ and thus remains a random function of the position. The average corner frequency over the fault is then calculated as $f_c = e \; v_{max}/(2\pi U) = e \times 1/(2\pi \times 0.14) = 3.1$ Hz, although
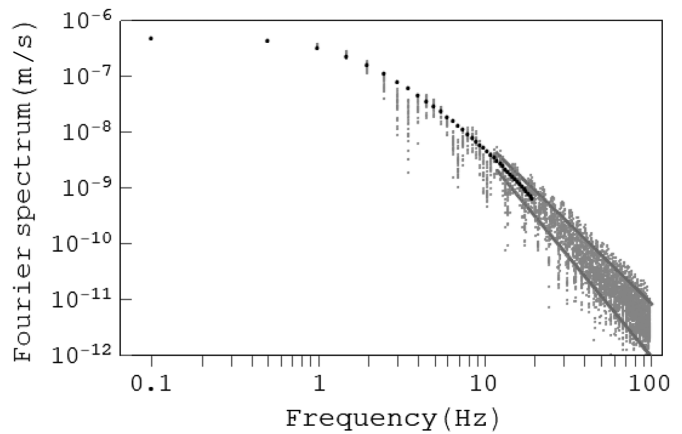

Figure 1. Amplitude spectra of radiated displacement from the asymptotic fault model for thirty different realizations of k-square slip. The two gray straight lines bracket the scatter of possible high-frequency slopes of the resulting spectra. The black dotted line represents the fitted spectrum of the equivalent omega-square point source with the high-cut filter kappa applied to it.

it is generally different at every point on the fault following equation (2).

We generated thirty independent realizations of the k^{-2} slip using the algorithm described and computed the radiated displacement spectrum from the narrow fault for all of them. Each realization generally has a different minimum and maximum slip; the only constraint is that they all need to share the same fault-average value. The thirty resulting spectra are plotted together in Figure 1; because they begin diverging to different slopes at relatively high frequencies, the band has been extended to 100 Hz. The two gray straight lines show the high-frequency slopes visually fitted to the end-member possibilities in the diverging "conical" area; their fall-off rates (the powers of frequency) are −2.9 and −3.6. The other cases are intermediate to these.

Two inferences can be made from Figure 1. First, the high-frequency slope predicted by equation (5) is −4. In the current more realistic simulation in which the corner frequency is allowed to vary across the fault, such an idealized scenario does not materialize. Now the various parts of the fault contribute radiation with randomly distributed corner frequencies, which adds up to the resulting spectrum with a variable slope, depending on a particular realization. Beresnev (2022b, his fig. 3), who randomly varied both $U(\xi)$ and $v_{max}(\xi)$ in equation (2), showed just two extreme cases for the linear fault, in which the two respective slopes were −1.5 and −2.6. The thirty random scenarios in Figure 1 not only confirm the slope variability but also illustrate that steeper decay should generally be expected.

Second, the spectral roll-off in all cases substantially exceeds −2 expected for the classic omega-square point source. This is the direct consequence of the finiteness of the causative fault.

The general physical explanation of the short-period decay is in the destructive interference of radiation emanating from different parts of the fault. Constructive interference only happens at very long wavelengths, at which the waves from the entire rupture add up in phase. The finite-fault effect, therefore, acts as a high-cut filter removing high frequencies from radiation.

It is well known that ground-motion modeling via omega-square point sources overpredicts the high-frequency content, requiring additional ad hoc filtering typically implemented through the adjustable kappa or f_{max} operators (Anderson and Hough, 1984; Boore, 2003, his equations 19 and 20). The true physical nature of such filtering is still debated; most often, it is attributed to the near-surface attenuation unaccounted for by the regular anelastic Q along the propagation path (Ktenidou *et al.*, 2014). There also are opinions that kappa is "an empirical parameter" "not measuring any specific physical phenomenon", arising from "great simplifications of complex source, path, and site effects" (Palmer and Atkinson, 2023, pp. 2666–2667).

Beresnev (2022b, 2023a) proposed to invoke the suppression of high frequencies by fault finiteness to explain the high-frequency decay as pure source effect, without resorting to ad hoc filtering. For example, the application of this approach allowed us to explain the short-period spectra of all well-recorded earthquakes from the Kiban–Kyoshin network in Japan in the magnitude range from 4 to 6 (Beresnev, 2023a). The same idea is illustrated in Figure 1. The black dotted line represents the spectrum radiated by an omega-square point source with the exactly same moment as that of the narrow fault at the same distance, multiplied by the kappa operator $\exp(-\pi\kappa f)$, fitted with $v_{max} = 0.5$ m/s and $\kappa = 0.025$ s. The fitting with κ was carried out to the frequency of 20 Hz, as typically done in the empirical determinations of this parameter (Boore and Joyner, 1997, their fig. 10). The black dotted line illustrates that the finite-fault radiation without additional filtering is equivalent to the point-source radiation with kappa. The inferred equivalent $\kappa = 0.025$ s is well within the range of the typical values reported in the literature. For example, Boore and Joyner (1997) deduced its generic value of 0.035 s for western North America.

Near field. Our investigation of the effect of varying distributions of k^{-2} slip on the radiation is continued with the near-field calculations. In all computations for the 1200 × 1200 m fault, v_{max} will be set to 0.25 m/s, keeping the average corner frequency unchanged at 3.1 Hz. The location-specific frequency, varying according to $U(\xi)$, is still obtained from equation (2). We will present the cases for both the coarse and fine resolutions. An example slip distribution for the coarse resolution is presented in Figure 2.

To sample the full variability, we set three hypocenter positions: in the middle of the vertical edge of the fault opposite to
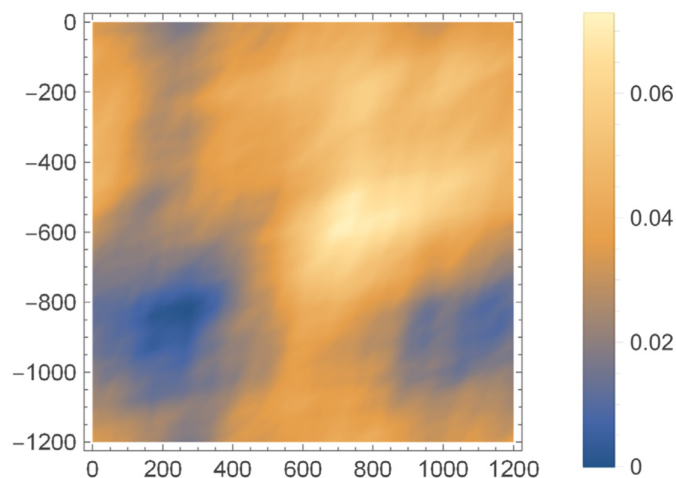

Figure 2. An example realization of coarse k^{-2} slip on a 1200 × 1200 m fault (the spatial sampling interval of 12 m). The horizontal and vertical axes are distances along length and width, respectively. The scale is a slip in meter. The color version of this figure is available only in the electronic edition.

the observation point (coordinates $\{L, 0, -W/2\}$), in the middle of the edge closest to the observation point (coordinates $\{0, 0, -W/2\}$), and in the center of the fault (coordinates $\{L/2, 0, -W/2\}$). These scenarios represent the end members of rupture directivity corresponding to the forward, reverse, and neutral cases. Testing the representative range of directivities by placing the hypocenter in three end-member locations is chosen rather than using an equivalent number of differently positioned observation stations. For each hypocenter position, we again generate thirty realizations of slip distribution for a total of ninety rupture scenarios. Figure 3 combines the spectra from all of them. Similarly to Figure 1, the two gray lines indicate the visually fitted end-member slopes: they are −2.7 and −4.0, consistent in the range with the far-field case of Figure 1.

Unlike Figure 1, the displacement spectra in Figure 3 do not flatten toward the lowest frequencies. This is the consequence of the presence of permanent ground displacement near the fault. In addition, the existence of an equivalent omega-square point source is impossible near the fault: the slip-velocity function (1), which describes the far-field displacement, does not contain the permanent component. The short-period decay seen is fully due to the source finiteness. One can nonetheless still attempt to formally fit a point-source spectrum having the same moment with the kappa operator applied to it to try to explain the observed fall-off. Because the kappa measurement only requires fitting the high-frequency part of the spectrum (Nye *et al.*, 2023), the respective formally determined slope with $\kappa = 0.040$ s is shown by the black dotted line. Similarly to Figure 1, this inferred κ has a practically plausible value. Again, in the case of real ground motions, the observed spectral slope can be deceptively construed as the result of kappa filtering, while in reality, as in Figure 3, it is purely due to finite-fault dimensions.
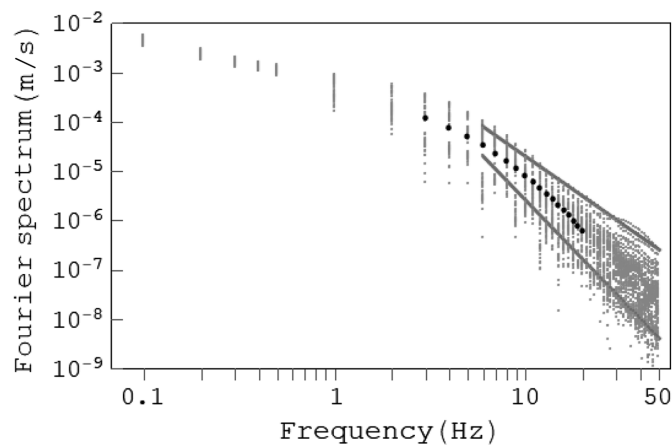
Figure 3. Amplitude spectra of radiated displacement from the 1200 × 1200 m coarse-resolution model at the point in the near field for three hypocenter end-member positions and thirty different *k*-square slip realizations for each. The meaning of the gray straight lines is the same as in Figure 1. The black dotted line represents the equivalent omega-square point source spectrum with the high-cut kappa filter applied to it, fitted to the high-frequency part of the resulting spectra.
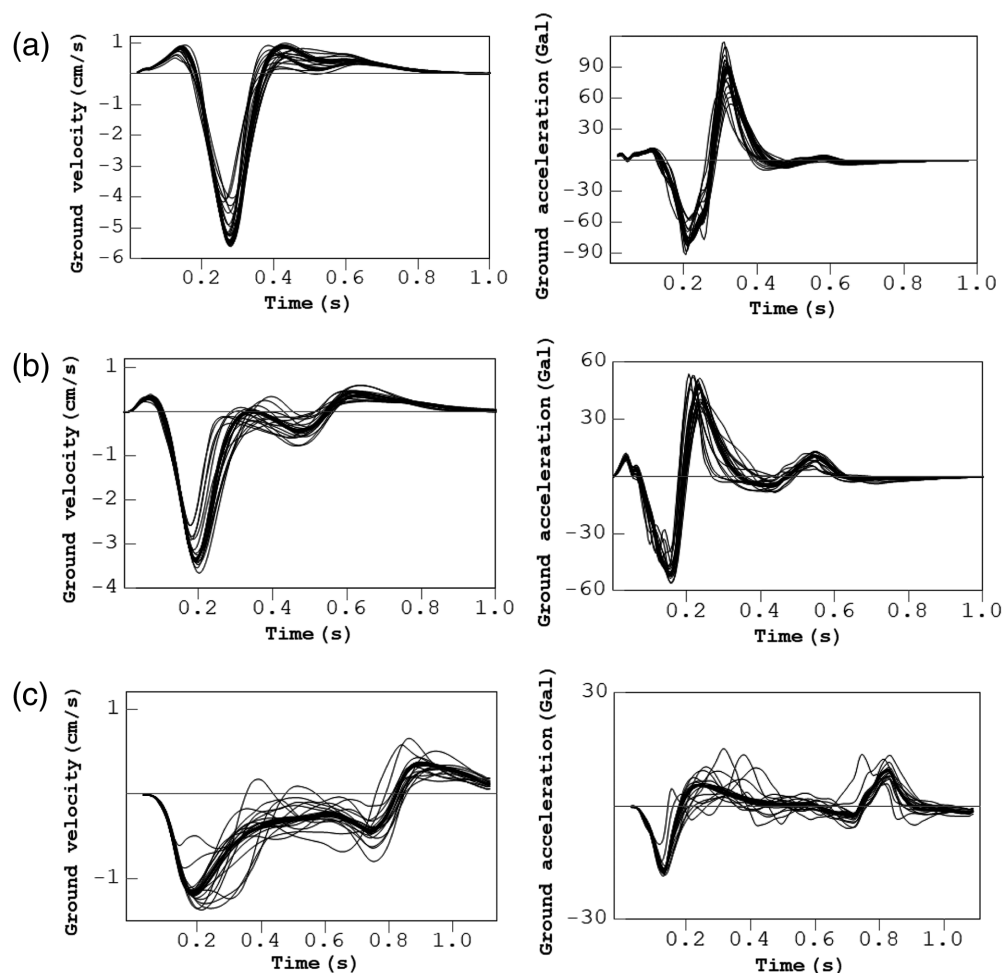
Figure 4 presents the time histories of ground velocity and acceleration, separately for the thirty realizations of the three directivity cases, illustrating the uncertainty in the time-domain ground motions due to natural variability in rupture scenarios. The normal differences between the types of directivity are clearly seen: short bursts of energy for the forward pulse (Fig. 4a) versus more protracted lower-amplitude waveforms backward (Fig. 4c). However, there is relatively little variation within a single directivity type due to alternative realizations of slip, except for the backward pulse. In the latter case (Fig. 4c), the scenario-by-scenario differences are in the later parts of the waveform, whereas the shapes of the steep arriving fronts in all cases are nearly independent of a particular fault-slip pattern. The latter fact is reflected in a relatively low variability in the peak values. The mean absolute values of peak ground velocity (PGV) for the cases of forward, neutral, and reverse propagation, respectively, are 5.1, 3.3, and 1.2 cm/s, with standard deviations of 0.49, 0.26, and 0.13 cm/s (10%, 8%, and 11% percent of the mean). For the peak ground acceleration (PGA), the means are 85.1, 51.6, and 17.2 Gal, with the standard deviations of 13.2, 1.9, and 0.97 Gal (16%, 4%, and 6% of the mean).

An example slip distribution for the fine resolution is presented in Figure 5. The difference with Figure 2 is that smaller heterogeneity can now be sampled in the slip on the fault plane. Figure 6 is the analog to Figure 3 for the fine-resolution case, and Figure 7 is the analog to Figure 4, with the difference that the time histories for the fine-resolution slip were calculated to the precision of five digits. The limiting slopes (gray lines) for the spectra in Figure 6 are −2.7 and −3.8. The black dotted line has the same kappa value of 0.040 s as in Figure 3. The mean absolute values of PGV for the cases of forward, neutral, and reverse propagation in Figure 7 are 5.2, 3.3, and 1.1 cm/s, respectively, with the standard deviations of 0.48, 0.25, and 0.16 cm/s (9%, 8%, and 15% of the mean). For the PGA, the means are 82.8, 50.3, and 16.7 Gal, with the standard deviations of 10.3, 4.0, and 1.6 Gal (12%, 8%, and 10% of the mean), respectively.
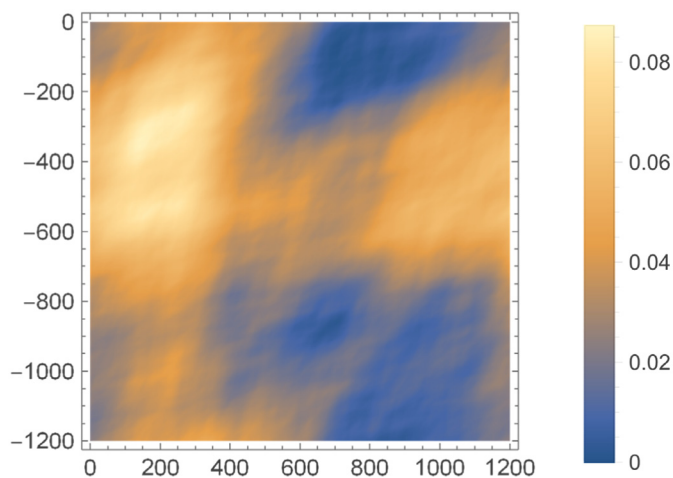

Figure 4. Ground-velocity (left) and acceleration (right) traces for the coarse-resolution model, *k*-square slip. (a) Forward, (b) neutral, and (c) reverse directivity cases, with thirty different realizations of *k*-square slip in each. The apparent thick lines are not separate graphs but the result of the clustering of several overlapping curves.

Figure 5. An example realization of fine k^{-2} slip on a 1200 × 1200 m fault (the spatial sampling interval of 6 m). The horizontal and vertical axes are distances along length and width, respectively. The scale is a slip in meter. The color version of this figure is available only in the electronic edition.
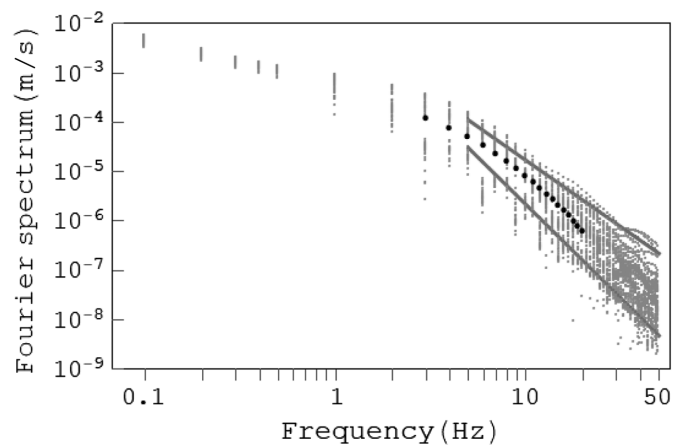

Figure 6. Amplitude spectra of radiated displacement from the 1200 × 1200 m fine-resolution model at the point in the near field for three end-member positions of the hypocenter and thirty different realizations of k-square slip for each. The meaning of the gray straight lines and the black dotted line is the same as in Figure 3.

All main inferences regarding the case of the finer slip remain unchanged relative to the coarser distribution: the cases are statistically indistinguishable. Considering that the ninety scenarios in the coarse- and fine-resolution cases were independently generated and thus different, we in addition conducted the following test. We produced a fine-resolution slip and then resampled it by taking every other slip value on the grid, thus increasing $\Delta\xi$ from 6 to 12 m. The hypocenter was in the middle of the fault. We then interpolated both distributions and computed the radiated spectra. On the scale of Figures 2 and 5, there was no visible difference between the two slip images. When plotted together on the scale of Figures 3 and 6, the spectra were also visually identical. This observation illustrates the fact that it is not the small-scale heterogeneity of slip that produces the high-frequency radiation. In this test, one of the slips is smoother, but the general pattern of the distribution of corner frequencies across the fault is still preserved. As a result, the same spectral slope is produced. The lack of conspicuous differences between the shapes of the spectra or the pulses emitted by faults with the difference in the smallest heterogeneity of a factor of two may have consequences for the ability of the slip-inversion algorithms to resolve the fine detail on the faults. Because there is no appreciable difference in the resulting seismic data, the details may be elusive for recognition.

Randomized model

To compare the signatures in the seismic fields, impressed by the strictly k^{-2} ruptures relative to randomly disturbed slip, we repeat the simulations leading to Figures 1, 3, and 4 (now for the coarse resolution only) for the randomized model.

Far-field of a narrow unidirectional rupture. We again begin with the far field of the narrow fault. The stochastic component that was superimposed on constant slip was in this case generated on a grid with the step of $L/99$; all other parameters are the same as for the k^{-2} narrow-fault simulation. Similarly to Figure 1, the spectra radiated by thirty different realizations are shown in Figure 8. The limiting slopes (gray lines) are −2.6 and −3.3; the kappa value of the black dotted line is 0.027 s. The single high-frequency slope predicted by equation (5) in this case is −3. It is reduced from −4 relative to the k-square model given the change in the term $U[\omega(\frac{\cos\Psi}{\beta} - \frac{1}{\nu})]$: the underlying slip is now constant, disturbed by the added white-like noise, but a constant has the spectral fall-off of negative one. However, as in Figure 1, this simple prediction does not materialize because of the same "heterogenization" of the spectral slope produced by the fluctuations of the corner frequency over the fault. Comparison between Figures 1 and 8 indicates that the radiated spectra between the two models are statistically indistinguishable: as long as the corner frequency is allowed to fluctuate, the specific form of the spatial spectrum of the final slip no longer controls the spectral behavior of radiation. A particular realization of spectral decay forms as a result of the incoherent superposition of waves from various parts of the rupture.

Near field. Figure 9 is the analog of Figure 3 now for the randomly disturbed constant slip, sharing all other parameters. The ninety realizations shown were generated for the same positions of the hypocenter. The slopes of the limiting gray lines are −3.0 and −3.8, and the kappa value for the black dotted line is 0.045 s.

Figure 10 is the analog to Figure 4 for the random model. The mean absolute values of PGV for the cases of forward, neutral, and reverse propagation are 5.3, 3.3, and 1.1 cm/s, respectively, with the standard deviations of 0.09, 0.04, and 0.04 cm/s (2%, 1%, and 4% of the mean). For the PGA, the means are
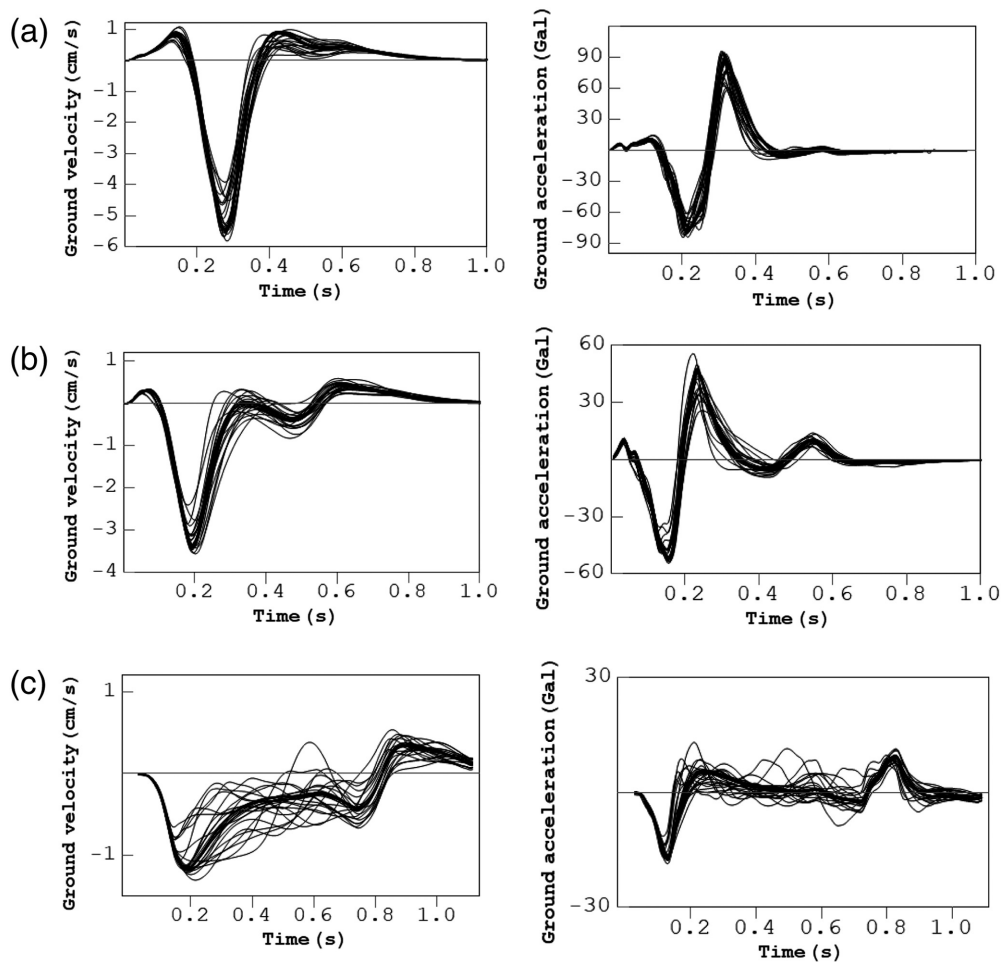
Figure 7. Ground-velocity (left) and acceleration (right) traces for the fine-resolution model, *k*-square slip. (a) Forward, (b) neutral, and (c) reverse directivity cases, with thirty different realizations of *k*-square slip in each. The apparent thick lines are not separate graphs but the result of the clustering of several overlapping curves.
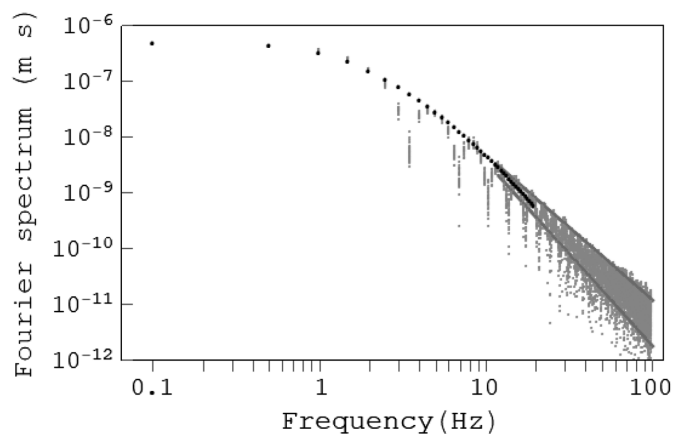
87.1, 50.5, and 17.2 Gal, with the standard deviations of 4.3, 1.6, and 0.6 Gal (5%, 3%, and 3% of the mean). What is noticeable is a much lesser variability in the waveforms from the randomized rupture in Figure 10 compared to the k^{-2} counterparts in Figures 4 and 7, although the spectra in Figures 3, 6, and 9 share a comparable diversity in the slopes. The average peak values of velocity and acceleration are nearly insensitive to a particular shape the distribution of slip takes: *k*-square or randomized constant.

In terms of the comparative spectral behavior between the k^{-2} and random slips (Figs. 3, 6, and 9), similarly to the far-field narrow-fault model, there is no statistical difference between all the slip models. The same explanation can be invoked: as long as the corner frequency is allowed to randomly fluctuate across the fault, the resulting incoherent summation overwhelms the otherwise distinctly different spectral decays that would

Figure 8. Amplitude spectra of radiated displacement from the asymptotic fault model for thirty different realizations of random slip. The meaning of the gray straight lines and the black dotted line is the same as in Figure 1.
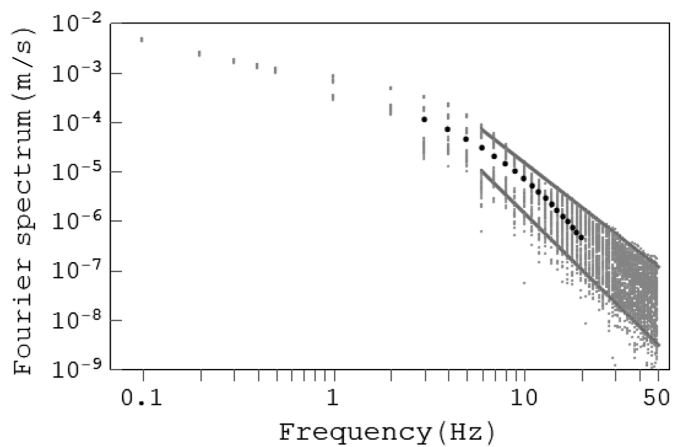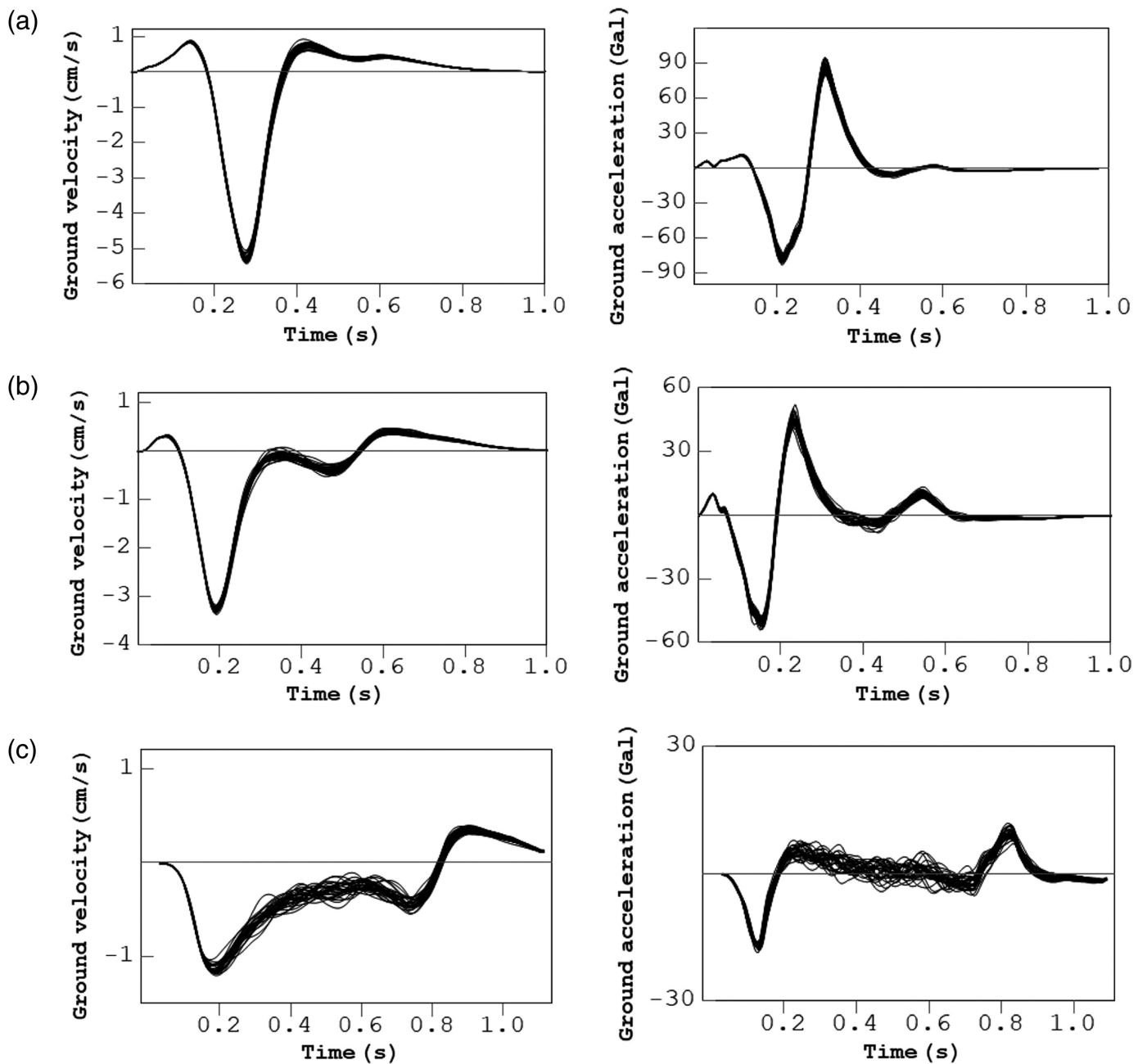

Figure 9. Amplitude spectra of radiated displacement from the 1200 × 1200 m model at the point in the near field for three end-member positions of the hypocenter and thirty different realizations of random slip. The meaning of the gray straight lines and the black dotted line is the same as in Figure 3.

(a)

(b)

(c)

Figure 10. Ground-velocity (left) and acceleration (right) traces for the random-slip model. (a) Forward, (b) neutral, and (c) reverse directivity cases, with thirty different realizations of randomized slip in each.

have resulted if the shape function $\Delta\dot{u}_s$ had been independent of the location and the slope had been fully controlled by equation (5).

Beresnev (2017a) also investigated the effect of introducing roughness into the static slip $U(\xi)$ and concluded that such randomization did not affect the radiated high-frequency spectra in any appreciable manner. The difference with the present study is that the earlier work only considered the shape function $\Delta\dot{u}_s$ independent of ξ. In that case, the high-frequency spectrum of radiation could be expected to be controlled by the spatial spectrum of slip as in equation (5), but the addition of a white-noise-like component to U does not change the slope of its spectrum. In the present study, both $U(\xi)$ and $\Delta\dot{u}_s(\xi,t)$ are allowed to be functions of the position: the

resulting fluctuations in the corner frequency at various ξ do affect the slope formation as we have seen in Figures 1, 3, 6, 8, and 9.

Crempien and Archuleta (2017) also investigated the effects of different spatially randomized kinematic rupture scenarios on the variability in the resulting ground motions. The important difference between their study and ours is that the authors enforced the ω-square shape of the emitted spectra (Crempien and Archuleta, 2017, p. 3456 and their fig. 7), whereas we

employ an ω-square slip-velocity function (equations 1 and 2) but let radiation from all the parts of the fault stack independently to form any shape of the resulting spectrum. As we have seen, the naturally forming slopes will then be significantly steeper than -2.

EFFECT OF IRREGULAR RUPTURE FRONTS

Until relatively recently, modelers typically assumed a constant value (usually, a fraction of β) of rupture-propagation velocity (e.g., Beresnev and Atkinson, 1997, 2002; Somerville et al., 1999, their table 1; Motazedian and Atkinson, 2005; Aagaard et al., 2008, p. 992; Ruiz et al., 2011; Infantino et al., 2020, p. 2564). Realistic fracture propagation is undoubtedly more complex, with a significant stochastic component added to the travel time. It has also become clear that assuming a smooth travel law creates artifacts of regular interference (Beresnev and Roxby, 2021).

It follows that including randomness in fracture travel should be a necessary feature of realistic earthquake models. However, the exact timing of the progression of cracks across fault planes has remained beyond the reach of source-dynamics inversions; there remains significant freedom in how to define irregular fronts. We avoid formulating specific dependences of rupture velocity on depth or its scaling with local slip, as in the model by, for example, Graves et al. (2008) and Graves and Pitarka (2010, their equations 4–6), as insufficiently constrained and will instead focus on pure effects of rupture-travel complexity excluding all other factors. To this end, a uniform slip will be considered.

Along with the form of the source time function and the slip distribution, a variable rupture velocity is another factor potentially affecting the high-frequency decay of seismic spectra. If the velocity changes in a smooth, nonstochastic fashion, a particular slope can be obtained in an ad hoc manner by constructing a specific timing of rupture travel. For the model of a small line source in the far field with a constant shape function, governed by equation (5), examples were supplied by Hisada (2000, the author's fig. 6) and Beresnev and Roxby (2021, their figs. 1 and 3a). In both studies, the addition of a stochastic component to rupture timing led to flattening of the high-frequency spectra by elimination of artifacts of orderly interference. Beresnev and Roxby (2021, their fig. 4b) corroborated this conclusion for the same 3D model as in the present study for the case of a constant shape function. They considered strictly circular ruptures, arrival for which was stochastically disturbed as they traveled.
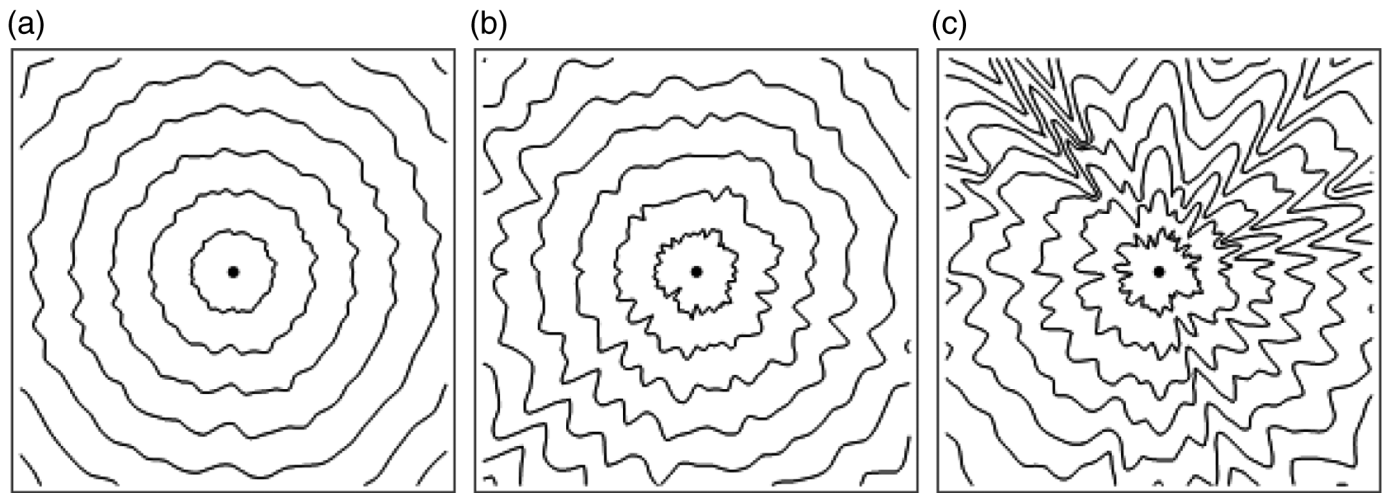
Graves et al. (2008) and Aagaard, Graves, Rodgers, et al. (2010) studied the effect of variable rupture velocity on radiation from large scenario earthquakes on the San Andreas fault. The frequencies greater than 1 Hz were simulated through the stochastic method. As noted earlier, this technique does not represent the near field accurately and suffers from the dependence on the subjective choice of the size of subfaults.

We continue exploring the effects of variable rupture speed using the full representation integral; the difference with the work of Beresnev and Roxby (2021) is that the requirement of concentric rupture fronts is eliminated: the travel is now anisotropic, with independent randomized velocity law constructed at each azimuth.

To isolate the pure effect of a geometrically irregular front, we consider the case of the 1200×1200 m fault with the uniform slip $U = 0.035$ m and $v_{\max} = 0.25$ m/s. The hypocenter is placed in the middle, corresponding to the case of "neutral" directivity. We thus sample the pure front-randomness effect. The observation point is in the near field as before. The travel-time complexity is introduced into $\Delta t(\xi)$ as follows. The full 360° in radial directions from the hypocenter were divided into 72 lines spaced at 5°. The diagonal of the fault was broken also into 72 equal intervals with the length Δr each, and the incremental travel time through each consecutive ith segment was calculated as $\Delta t_i = \Delta r/[v(1 + \eta)]$. The constant velocity v was set to 0.8β. The random variable η was drawn from the normal distribution with zero mean and the desired standard deviation, constrained to equal -0.9 if it accidentally fell below or was equal to -1. A slight departure from the similar algorithm of generating η for the randomized slip distributions was needed to avoid infinite values of Δt_i. Considering the standard deviations tested below, the value of $\eta = -1$ was highly unlikely and probably never materialized. In addition, if $v(1 + \eta)$ exceeded 1.5β, it was kept at 1.5β, allowing supershear propagation. This procedure was repeated for all 72 azimuthal directions. A new η was drawn each time the travel time was advanced through each segment Δr, independently in all the azimuths. The process resulted in an azimuthally anisotropic and temporally disordered discrete travel-time function $\Delta t(r_i, \varphi_j)$ on a grid in the polar coordinates with the center at the rupture-initiation point. This function was then interpolated with a third-order polynomial to produce a smooth distribution of travel time to a desired point $\{r, \varphi\}$ on the fault. To obtain the distribution $\Delta t(\xi)$ needed for the integration in equation (3), the polar coordinates of a point were converted into the Cartesian $\{\xi_1, \xi_3\}$.

Three values of the standard deviation in η were tested: 0.1, 0.2, and 0.3. The resulting rupture fronts are depicted in Figure 11. The shape of the contour for every particular azimuth is probably mostly affected by a single large fluctuation in η, which is then preserved for all subsequent propagation distances along the azimuth. Figure 12 presents the respective radiated spectra, ground velocities, and ground accelerations, together with the case of zero standard deviation (radial travel with constant velocity). For the irregular rupture fronts, the spectra were calculated to the precision of two and the traces to the precision of three digits.

The spectra in Figure 12 are coded by the same color: there is no visible difference between them, except for random scatter. The decay of the fitting straight line is -3.5, and the

(a)   (b)   (c)

Figure 11. Geometry of the rupture fronts corresponding to the three values of standard deviation in the random variable η: (a) 0.1, (b) 0.2, and (c) 0.3. The contour lines are spaced at 50 ms. The fault representation is as in Figures 2 and 5.

parameter kappa of the black dotted line is 0.045 s. On the other hand, the velocity and acceleration traces in the case of the standard deviation of 0.3 (the gray lines in Fig. 12) are conspicuously different from the other three. Significant irregularity in the rupture velocity is thus seen to affect the resulting ground velocity and acceleration to a much greater extent than the frequency spectra. This result is opposite to what we have seen as the effect of the irregular distribution of slip, in which case the slip complexity distinctly disturbed the spectral slopes but not the shapes of the pulses (Figs. 1, 3, 4, and 6–10). The sharpness of the pulses in Figure 12 in the case of the largest irregularity is reduced, blurring the effect of directivity. The same reduction in the contrast between the forward- and reverse-radiated pulses by irregular rupture travel was noted by Beresnev (2021), where strictly circular ruptures with randomly varying velocities were considered.

The absence of the effect of anisotropic disorderly rupture propagation on the resulting frequency spectra, with respect to travel with constant velocity, does not agree with the way randomized travel distinctly flattened the slopes of the spectra in our previous work (Beresnev and Roxby, 2021, their fig. 4b). The only difference between the two studies is that concentric (isotropic) fronts with stochastically disturbed timing were considered previously, while anisotropic, geometrically chaotic fronts have been presently allowed, as shown in Figure 11. The only explanation that we can invoke at this time is that orderly circular fronts, even if accelerating/decelerating in a chaotic fashion, still produce radiation that correlates over different parts of the fault, creating quasi-regular interference and forming specific spectral slopes. True randomness of the geometrically incoherent fronts does not add any constant value to the spectral decay, as compared to the case of the constant rupture velocity (0.8β in our case) (Fig. 12), except supplying a purely random scatter. The effect on the velocity and acceleration traces is substantial, though. A conclusion, of value to future simulations, is that the way the rupture progression along the fault plane is randomized is important in forming the resulting

seismic spectral behavior. Because there is no unique way to introduce such randomness (e.g., compare our Fig. 11 with fig. 1 of Graves and Pitarka, 2016), this line of study should be continued.

A limiting factor on the possible complexity of the rupture process in our study, being based on the exact mathematical computation of the representation integral, is the required numerical precision that needs to be maintained. Beyond a certain level of heterogeneity, the integral stops converging to a reasonable number of digits.

EFFECT OF SLIP VELOCITY

A conclusion from our earlier studies (Beresnev, 2017a, his figs. 6 and 7; Beresnev, 2022a, his fig. 7) is that the parameter v_{max} of the slip-velocity function exerts a predominant influence on the strength of high-frequency radiation for both the general omega-n and dynamically compatible functions. This is explained by the strong power-of-n dependence of the high-frequency spectral level on v_{max}. For example, the omega-square spectrum of the function $\Delta\dot{u}(\xi,t)$ in equation (1) at $\omega \gg \omega_c$ reduces to

$$|\Delta\dot{u}(\xi,\omega)| = e^2 \frac{v_{max}^2}{U} \omega^{-2}, \qquad (8)$$

that is, the spectrum scales as v_{max}^2 (Beresnev, 2022a, his equation 24). We verify this inference using the present approach, in which the general variability in the corner frequency in $\Delta\dot{u}(\xi,t)$ over the finite-fault plane, as in equations (2) and (3), is allowed. To that effect, we fix a single realization of the k-square slip with the hypocenter in the middle of the fault and compare the radiation for two v_{max} values 0.25 and 1 m/s at the same observation point in the near field as before. The corner frequency is
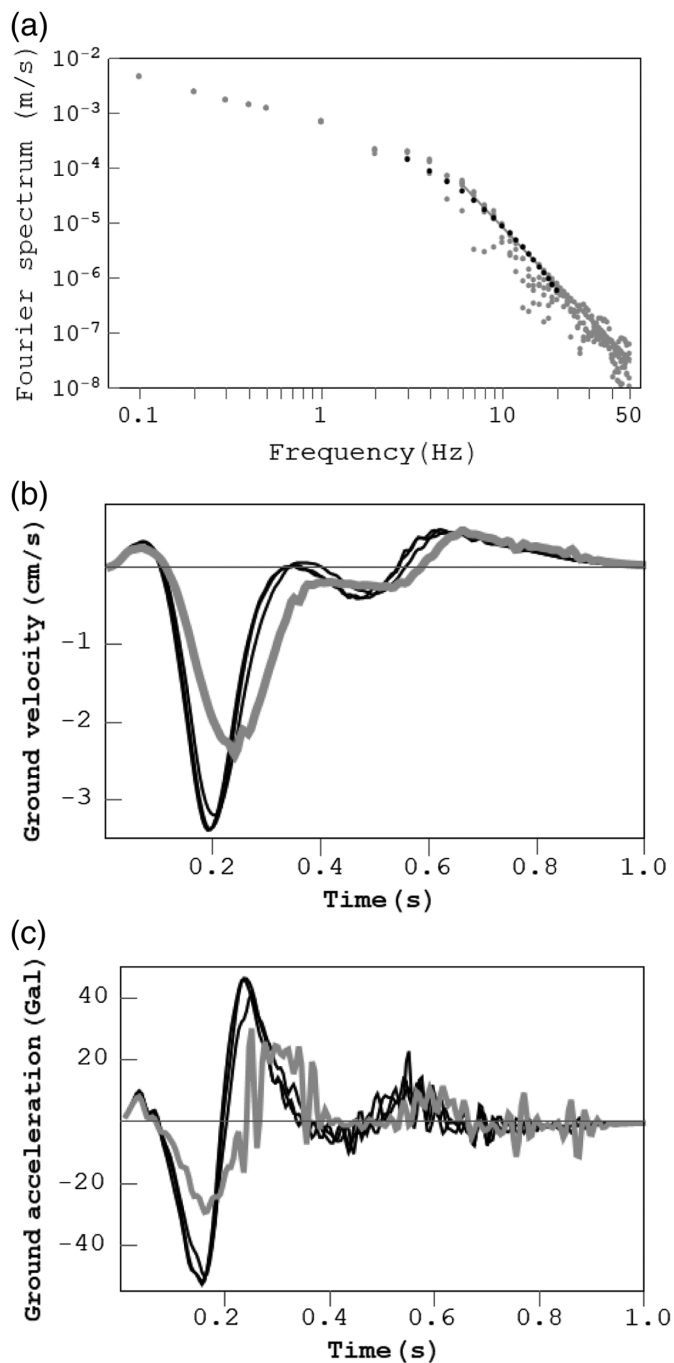
(a)

(b)

(c)

Figure 12. (a) The amplitude spectra of radiated displacement, (b) the ground-velocity traces, and (c) the ground-acceleration traces corresponding to the constant-velocity case and the three rupture fronts in Figure 11. The gray straight line in the spectra indicates the high-frequency slope. The meaning of the black dotted line in the spectra is the same as in Figure 3. The gray velocity and acceleration traces correspond to the greatest standard deviation of 0.3 in the random variable η.

randomly varying, inversely proportional to $U(\xi)$ as per equation (2). According to the theoretical quadratic dependence (equation 8) of the spectral level on v_{max}, we expect that the high-frequency spectra will be different by approximately a factor of sixteen.

Figure 13 depicts the spectra, their ratio, and the traces corresponding to the two slip-velocity values, all other parameters being the same. The near-field high-frequency spectra behave as expected: their ratio fluctuates around the predicted value of sixteen, shown by a straight dotted line for reference. The increase in v_{max} boosts the time-domain characteristics of ground motion: the PGV increases from 3.1 to 6.6 cm/s, and the PGA increases from 47 to 175 Gal. Recall that the entire diversity of possible k-square slips, for the same central hypocenter position as here, led to the variation in PGVs and PGAs of less than ten percent, as measured as standard deviation divided by the mean.

From our experience, the conclusion that v_{max} is the most influential parameter does not depend on the particular choice among the common source time functions in a broad range tested. Beresnev (2022a, his fig. 7) showed the same quadratic dependence of the high-frequency spectra on v_{max}, as in equation (8), for both the ω^{-2} and Guatteri et al. slips. In a different study (Beresnev, 2024), we compared the effect on the traces of ground displacement, velocity, and acceleration computed for the same point in the near field as in the present work. Three fault sizes were considered corresponding to M_w 4, 5, and 6 earthquakes. For each, radiation was calculated for three slip functions: the dynamically compatible one of Liu et al. (2006) (a smooth version of the Guatteri et al. case), the omega-square ($n = 2$), and the omega-cube ($n = 3$) shapes. They all were assigned the identical values of the parameters U and v_{max}. For all the faults, once these defining parameters were fixed, all the slip functions led to indiscernible differences in the radiated time histories in the frequency band up to 45 Hz.
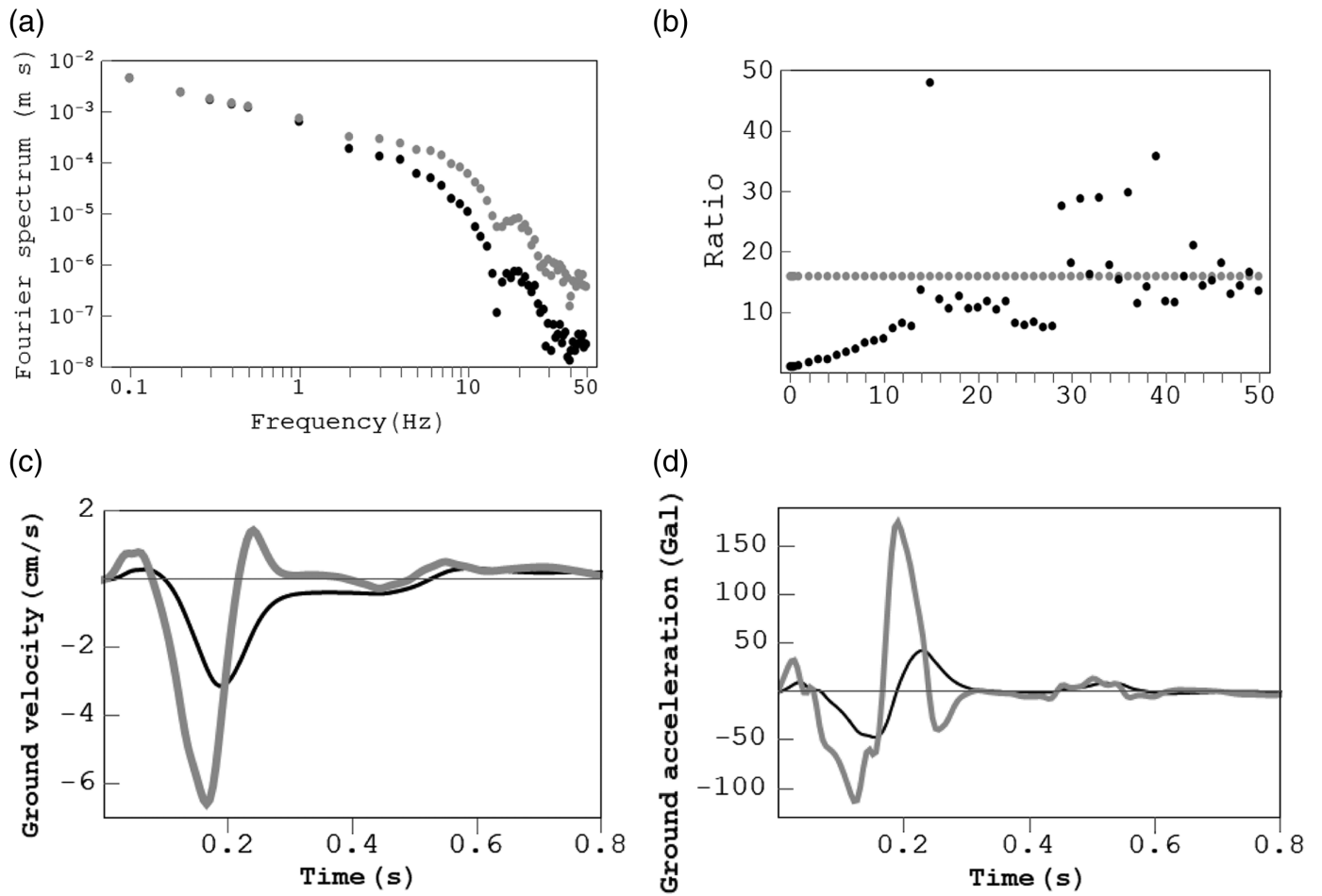
Linear matrix inversions of seismic and geodetic data for slip distributions on earthquake faults commonly use the representation of the slip-rate function by isosceles triangles (e.g., Lay et al., 2011; Yoshida et al., 2011; Zhu et al., 2022). The temporal shape of the ground-velocity pulse is controlled by the second derivative of the triangle,

$$\Delta \ddot{u}(t) = \frac{v_{max}^2}{U}, \quad 0 \le t < \frac{T}{2}, \tag{9a}$$

$$\Delta \ddot{u}(t) = -\frac{v_{max}^2}{U}, \quad \frac{T}{2} \le t < T, \tag{9b}$$

in which T is the total duration (Beresnev, 2023b, his equations 4a and 4b). A popular method of nonlinear inversion, which simultaneously solves for several unknown rupture parameters by minimizing an objective function (e.g., Hayes, 2017; Koch et al., 2019; Goldberg et al., 2022), employs the technique of Ji et al. (2002) that in turn uses the slip-rate form of a cosine

$$\Delta \dot{u}(t) = U \frac{1 - \cos(2\pi t/T)}{T}, \tag{10}$$

(a) [figure]
(b) [figure]
(c) [figure]
(d) [figure]

Figure 13. (a) Amplitude spectra of radiated displacement, (b) their ratio, (c) the ground-velocity traces, and (d) the ground-acceleration traces corresponding to the values of maximum slip velocity $v_{\max} = 0.25$ (black color in the spectra and traces) and 1 m/s (gray color). The horizontal dotted line in the ratio shows the reference value of sixteen.

(Ji *et al.*, 2002, their equation 2). The second derivative is

$$\Delta\ddot{u}(t) = 2\pi \frac{U}{T^2} \sin\left(2\pi \frac{t}{T}\right). \qquad (11)$$

For both the triangular slip in equation (9) and the cosine form in equation (11), the duration is the proxy for the slip velocity through the same formula $T = 2U/v_{\max}$. Substituting into equation (11) gives

$$\Delta\ddot{u}(t) = \frac{\pi}{2} \frac{v_{\max}^2}{U} \sin\left(2\pi \frac{t}{T}\right). \qquad (12)$$

One can see that, given that ground velocity is controlled by high frequencies, the factor $v_{\max}^2/U$ universally appears in all measures of high-frequency radiation, both in the spectral (as in equation 8) and temporal (as in equations 9 and 12) domains, for all the popular source time functions that we have analyzed. The same factor appears in the temporal representation of the omega-square ground-velocity pulse (Beresnev, 2023b, his equation 5). The quadratic dependence of the high-frequency levels on the maximum rate of slip and hence the dominant effect of $v_{\max}$ on radiation comes out as a universal conclusion.

CONCLUSIONS

Our goal has been to document the variability in frequency- and time-domain characteristics of ground motions in kinematic simulations caused by the uncertainty in the rupture scenarios. The rupture characteristics investigated include the postulated distribution of static slip, the geometry of the rupture fronts, and the maximum rate of slip. We have used the omega-square slip-velocity function (equation 1), in which the corner frequency was allowed to randomly vary across the fault as it would in all realistic situations (equation 2).

It is known that the high-frequency roll-off of the Fourier spectra, radiated into the far field by small 1D sources, in the case of the identical temporal shape of the slip-velocity function over the entire fault, is controlled by the spatial spectrum of the slip distribution, as exemplified by equation (5). In this situation, the corner frequency is constant everywhere. However, in the more realistic scenarios of $\Delta\dot{u}(\boldsymbol{\xi},t)$ changing over the fault,

the control of the Fourier spectral decay by the shape of the wavenumber spectrum of slip is lost in both the near and far fields. The same natural variability in the spectral slopes, between roughly -2.5 and -4.0 (the power of frequency), is observed for multiple realizations of both k^{-2} and randomly perturbed slip. This behavior is explained by the heterogenization of the corner frequency over different parts of the fault, with a particular slope at the observation point forming as a result of the summation of radiation with a variety of corner frequencies. The slope is not affected by two different spatial resolutions of the same slip, changed by a factor of two in our case.

The steep decay rates in the high-frequency spectra, substantially exceeding the fall-off of -2 of the underlying slip-velocity function, can explain the additional high-cut filtering that is required in modeling strong-motion radiation through omega-square point sources. It is well known that in the latter case, the application of kappa or $f_{\max}$ operators is needed to artificially reduce the spectra to greater decays. However, the combination of finite-fault geometry and heterogeneous slip has the same effect on the radiated fields as a formal kappa operator with κ ranging from ~ 0.025 to 0.045 s, without the need for additional filtering. Such kappa values are well in the typically reported range; for example, the values experimentally measured in the San Francisco Bay area by Nye *et al.* (2023, caption to their fig. 4) mostly fall within 0.028 and 0.045 s. Parolai (2018) proposed to explain the same kappa filtering by scattering on near-surface heterogeneities; however, the study did not quantify whether the resulting extra decay was in the range of the typical values of this parameter.

Even though all examples have been generated for either M_{w} 4 or 5 faults, the inferred fall-off rates, equivalent to kappa filtering, are not expected to be magnitude dependent. For example, in the case of the unidirectional line rupture moving with constant speed, when the slip is constant, the slope of $U[\omega(\frac{\cos \Psi}{\beta} - \frac{1}{v})]$ in equation (5) changes to -1 (Aki and Richards, 1980, p. 810). This additional fault-finiteness-induced decay is independent of the size of the fault.

The variability in peak ground motions is insignificant throughout all k^{-2} or random ruptures in the set of scenarios considered. For the same hypocenter position, the variations in peak velocities and accelerations from one realization to another, expressed as the ratio of standard deviation to the mean, are under $\sim 15\%$ for all the slip types, be it random or k^{-2}. There is no statistical difference between the frequency and time domain characteristics of radiation from k^{-2} or purely random distributions, in both near and far fields.

The coarse and fine k^{-2} slip models, in which the size of the smallest detail is different by a factor of two, produce indistinguishable spectra and waveforms. This fact may have adverse consequences for the ability of waveform-inversion algorithms for slip distributions to resolve details on earthquake faults.

Unlike the slip distributions, the geometric complexity of the rupture fronts, in which ruptures chaotically accelerate and slow down in various directions, does not affect the slopes of the radiated spectra, at least in the examples considered. However, increasing irregularity is seen to blur the fault's directivity in the sense of reducing the sharpness of radiated pulses.

Although a specific choice of slip distribution and its fine structure exert a minor effect on the peak values of the resulting ground motions, the choice of the peak slip velocity has an overwhelming influence. The PGA increases in about the same proportion as the average $v_{\max}$ on the fault. Spatial heterogeneity is not required to produce extreme ground motions: even ruptures with constant slip can do so (Beresnev,2022c). A compilation of literature sources suggests that peak slip velocities may lie in the range of ~ 0.1–2 m/s (Anil-Bayrak and Beresnev, 2009; Anderson, 2010; Beresnev, 2022c); that is, they may change by a factor of 20 or even beyond. A focus of future observational effort should be directed toward better constraining the realistic range of change in this parameter: this is where the greatest uncertainty in the forecasted peak ground motions may reside.

The fact that the results of this study have been obtained for the faults corresponding to M 4 and 5 earthquakes is motivated by the need to achieve the required precision of the evaluation of the representation integral with highly variable integrands. However, because the conclusions are naturally explained by the physical shape of the slip function and the effects of geometric interference, they are not expected to substantially change if the dimensions of the fault are increased.

DATA AND RESOURCES

DECLARATION OF COMPETING INTERESTS

ACKNOWLEDGMENTS

REFERENCES

Aagaard, B. T., and T. H. Heaton (2004). Near-source ground motions from simulations of sustained intersonic and supersonic fault ruptures, *Bull. Seismol. Soc. Am.* **94,** 2064–2078.

Aagaard, B. T., T. M. Brocher, D. Dolenc, D. Dreger, R. W. Graves, S. Harmsen, S. Hartzell, S. Larsen, and M. L. Zoback (2008). Ground-motion modeling of the 1906 San Francisco earthquake, Part I: Validation using the 1989 Loma Prieta earthquake, *Bull. Seismol. Soc. Am.* **98,** 989–1011.

Aagaard, B. T., R. W. Graves, A. Rodgers, T. M. Brocher, R. W. Simpson, D. Dreger, N. A. Petersson, S. C. Larsen, S. Ma, and R. C. Jachens (2010). Ground-motion modeling of Hayward fault

scenario earthquakes, Part II: Simulation of long-period and broadband ground motions, *Bull. Seismol. Soc. Am.* **100,** 2945–2977.

Aagaard, B. T., R. W. Graves, D. P. Schwartz, D. A. Ponce, and R. W. Graymer (2010). Ground-motion modeling of Hayward fault scenario earthquakes, Part I: Construction of the suite of scenarios, *Bull. Seismol. Soc. Am.* **100,** 2927–2944.

Aki, K., and P. G. Richards (1980). *Quantitative Seismology*, W. H. Freeman and Company, San Francisco.

Anderson, J., and S. Hough (1984). A model for the shape of the Fourier amplitude spectrum of acceleration at high frequencies, *Bull. Seismol. Soc. Am.* **74,** 1969–1993.

Anderson, J. G. (2010). Source and site characteristics of earthquakes that have caused exceptional ground accelerations and velocities, *Bull. Seismol. Soc. Am.* **100,** 1–36.

Anil-Bayrak, N. A., and I. A. Beresnev (2009). Fault slip velocities inferred from the spectra of ground motions, *Bull. Seismol. Soc. Am.* **99,** 876–883.

Beresnev, I. (2013). Reflections on frequency dependence in earthquake-source inversions, *Nat. Hazards* **66,** 1287–1291.

Beresnev, I. A. (2001). What we can and cannot learn about earthquake sources from the spectra of seismic waves, *Bull. Seismol. Soc. Am.* **91,** 397–400.

Beresnev, I. A. (2003). Uncertainties in finite-fault slip inversions: To what extent to believe? (A critical review), *Bull. Seismol. Soc. Am.* **93,** 2445–2458.

Beresnev, I. A. (2017a). Factors controlling high-frequency radiation from extended ruptures, *J. Seismol.* **21,** 1277–1284.

Beresnev, I. A. (2017b). Simulation of near-fault high-frequency ground motions from the representation theorem, *Pure Appl. Geophys.* **174,** 4021–4034.

Beresnev, I. A. (2021). The effects of variable velocity of rupture propagation on fault's directivity pulses, *Pure Appl. Geophys.* **178,** 3427–3439.

Beresnev, I. A. (2022a). Equivalence between ω^n source time functions and those proposed from dynamic finite-source modeling, *Bull. Seismol. Soc. Am.* **112,** 1886–1893.

Beresnev, I. A. (2022b). Spatial heterogeneity of fault slip and the radiated spectra of ground motions, *Bull. Seismol. Soc. Am.* **112,** 1463–1471.

Beresnev, I. A. (2022c). The strongest possible earthquake ground motion, *J. Earthq. Eng.* **26,** 563–572.

Beresnev, I. A. (2023a). A method to simulate high-frequency decay of acceleration spectra of ground motions without the need of kappa or f_{max} filters, *Bull. Seismol. Soc. Am.* **113,** 1115–1132.

Beresnev, I. A. (2023b). Uncertainties in finite-fault slip inversions, Part II: Fault discretization and parameterization of slip function, *Pure Appl. Geophys.* **180,** 59–68.

Beresnev, I. A. (2024). Choices of slip function and simulated ground motions, *Pure Appl. Geophys.* **181,** 1859–1869, doi: 10.1007/s00024-024-03502-3.

Beresnev, I. A., and G. M. Atkinson (1997). Modeling finite-fault radiation from the ω^n spectrum, *Bull. Seismol. Soc. Am.* **93,** 67–84.

Beresnev, I. A., and G. M. Atkinson (2002). Source parameters of earthquakes in eastern and western North America based on finite-fault modeling, *Bull. Seismol. Soc. Am.* **92,** 695–710.

Beresnev, I. A., and K. Roxby (2021). The effects of variable and constant rupture velocity on the generation of high-frequency radiation from earthquakes, *Pure Appl. Geophys.* **178,** 1157–1164.

Boore, D. M. (2003). Simulation of ground motion using the stochastic method, *Pure Appl. Geophys.* **160,** 635–676.

Boore, D. M., and W. B. Joyner (1997). Site amplifications for generic rock sites, *Bull. Seismol. Soc. Am.* **87,** 327–341.

Bray, J. D., and A. Rodriguez-Marek (2004). Characterization of forward-directivity ground motions in the near-fault region, *Soil Dynam. Earthq. Eng.* **24,** 815–828.

Crempien, J. G. F., and R. J. Archuleta (2017). Within-event and between-events ground motion variability from earthquake rupture scenarios, *Pure Appl. Geophys.* **174,** 3451–3465.

Dreger, D. S., and T. H. Jordan (2015). Introduction to the focus section on validation of the SCEC broadband platform v.14.3 simulation methods, *Seismol. Res. Lett.* **86,** 15–16.

Fayjaloun, R., M. Dabaghi, C. Cornou, M. Causse, Y. Lu, L. Stehly, C. Voisin, and A. Mariscal (2021). Hybrid simulation of near-fault ground motion for a potential M_w 7 earthquake in Lebanon, *Bull. Seismol. Soc. Am.* **111,** 2441–2462.

Gallovič, F., and J. Brokešová (2004). On strong ground motion synthesis with k^{-2} slip distributions, *J. Seismol.* **8,** 211–224.

Goldberg, D. E., P. Koch, D. Melgar, S. Riquelme, and W. L. Yeck (2022). Beyond the teleseism: Introducing seismic and geodetic data into routine USGS finite-fault modeling, *Seismol. Res. Lett.* **93,** 3308–3323.

Graves, R., and A. Pitarka (2016). Kinematic ground-motion simulations on rough faults including effects of 3D stochastic velocity perturbations, *Bull. Seismol. Soc. Am.* **106,** 2136–2153.

Graves, R. W., and A. Pitarka (2010). Broadband ground-motion simulation using a hybrid approach, *Bull. Seismol. Soc. Am.* **100,** 2095–2123.

Graves, R. W., B. T. Aagaard, K. W. Hudnut, L. M. Star, J. P. Steward, and T. H. Jordan (2008). Broadband simulations for M_w 7.8 southern San Andreas earthquakes: Ground motion sensitivity to rupture speed, *Geophys. Res. Lett.* **35,** L22302, doi: 10.1029/2008GL035750.

Guatteri, M., P. M. Mai, and G. C. Beroza (2004). A pseudo-dynamic approximation to dynamic rupture models for strong ground motion prediction, *Bull. Seismol. Soc. Am.* **94,** 2051–2063.

Hayes, G. P. (2017). The finite, kinematic rupture properties of great-sized earthquakes since 1990, *Earth Planet. Sci. Lett.* **468,** 94–100.

Herrero, A., and P. Bernard (1994). A kinematic self-similar rupture process for earthquakes, *Bull. Seismol. Soc. Am.* **84,** 1216–1228.

Hisada, Y. (2000). A theoretical omega-square model considering the spatial variation in slip and rupture velocity, *Bull. Seismol. Soc. Am.* **90,** 387–400.

Infantino, M., I. Mazzieri, A. G. Özcebe, R. Paolucci, and M. Stupazzini (2020). 3D physics-based numerical simulations of ground motion in Istanbul from earthquakes along the Marmara segment of the North Anatolian fault, *Bull. Seismol. Soc. Am.* **110,** 2559–2576.

Ji, C., D. J. Wald, and D. V. Helmberger (2002). Source description of the 1999 Hector Mine, California, earthquake, Part I: Wavelet domain inversion theory and resolution analysis, *Bull. Seismol. Soc. Am.* **92,** 1192–1207.

Koch, P., F. Bravo, S. Riquelme, and J. G. F. Crempien (2019). Near-real-time finite-fault inversions for large earthquakes in Chile using strong-motion data, *Seismol. Res. Lett.* **90,** 1971–1986.

Ktenidou, O.-J., F. Cotton, N. A. Abrahamson, and J. G. Anderson (2014). Taxonomy of κ: A review of definitions and estimation approaches targeted to applications, *Seismol. Res. Lett.* **85,** 135–146.

Lay, T., C. J. Ammon, H. Kanamori, L. Xue, and M. J. Kim (2011). Possible large near-trench slip during the 2011 M_w 9.0 off the Pacific coast of Tohoku earthquake, *Earth Planets Space* **63,** 687–692.

Lee, R. L., B. A. Bradley, P. J. Stafford, R. W. Graves, and A. Rodriguez-Marek (2020). Hybrid broadband ground motion simulation validation of small magnitude earthquakes in Canterbury, New Zealand, *Earthq. Spectra* **36,** 673–699.

Liu, P., R. J. Archuleta, and S. H. Hartzell (2006). Prediction of broadband ground-motion time histories: Hybrid low/high-frequency method with correlated random source parameters, *Bull. Seismol. Soc. Am.* **96,** 2118–2130.

Mai, P. M., and G. C. Beroza (2002). A spatial random field model to characterize complexity in earthquake slip, *J. Geophys. Res.* **107,** 2308, doi: 10.1029/2001JB000588.

Motazedian, D., and G. Atkinson (2005). Stochastic finite-fault modeling based on a dynamic corner frequency, *Bull. Seismol. Soc. Am.* **95,** 995–1010.

Nye, T., V. J. Sahakian, E. King, A. Baltay, and A. Klimasewski (2023). Estimates of κ_0 and effects on ground motions in the San Francisco Bay area, *Bull. Seismol. Soc. Am.* **113,** 823–842.

Palmer, S. M., and G. M. Atkinson (2023). Uncertainties in broadband determination of the high-frequency spectral decay, kappa, in eastern Canada, *Bull. Seismol. Soc. Am.* **113,** 2666–2688.

Parolai, S. (2018). κ_0: Origin and usability, *Bull. Seismol. Soc. Am.* **108,** 3446–3456.

Pitarka, A., A. Akinci, P. De Gori, and M. Buttinelli (2022). Deterministic 3D ground-motion simulations (0-5 Hz) and surface topography effects of the 30 October 2016 M_w 6.5 Norcia, Italy, earthquake, *Bull. Seismol. Soc. Am.* **112,** 262–286.

Pitarka, A., R. Graves, K. Irikura, K. Miyakoshi, C. Wu, H. Kawase, A. Rodgers, and D. McCallen (2022). Refinements to the Graves-Pitarka kinematic rupture generator, including a dynamically consistent slip-rate function, applied to the 2019 M_w 7.1 Ridgecrest earthquake, *Bull. Seismol. Soc. Am.* **112,** 287–306.

Razafindrakoto, H. N. T., F. Cotton, D. Bindi, M. Pilz, R. W. Graves, and S. Bora (2021). Regional calibration of hybrid ground-motion simulations in moderate seismicity areas: Application to the Upper Rhine graben, *Bull. Seismol. Soc. Am.* **111,** 1422–1444.

Rodgers, A. J., N. A. Petersson, A. Pitarka, D. B. McCallen, B. Sjorreen, and N. Abrahamson (2019). Broadband (0-5 Hz) fully deterministic 3D ground-motion simulations of a magnitude 7.0 Hayward fault earthquake: Comparison with empirical ground-motion models and 3D path and site effects from source normalized intensities, *Seismol. Res. Lett.* **90,** 1268–1284.

Rodgers, A. J., A. Pitarka, R. Pankajakshan, B. Sjögreen, and N. A. Petersson (2020). Regional-scale 3D ground-motion simulations of M_w 7 earthquakes on the Hayward fault, northern California resolving frequencies 0-10 Hz and including site-response corrections, *Bull. Seismol. Soc. Am.* **110,** 2862–2881.

Ruiz, J. A., D. Baumont, P. Bernard, and C. Berge-Thierry (2011). Modelling directivity of strong ground motion with a fractal, k^{-2}, kinematic source model, *Geophys. J. Int.* **186,** 226–244.

Schmedes, J., and R. J. Archuleta (2008). Near-source ground motion along strike-slip faults: Insights into magnitude saturation of PGV and PGA, *Bull. Seismol. Soc. Am.* **98,** 2278–2290.

Schmedes, J., R. J. Archuleta, and D. Lavallée (2013). A kinematic rupture model generator incorporating spatial interdependency of earthquake source parameters, *Geophys. J. Int.* **192,** 1116–1131.

Skarlatoudis, A. A., P. G. Somerville, H. K. Thio, and J. R. Bayless (2015). Broadband strong ground motion simulations of large subduction earthquakes, *Bull. Seismol. Soc. Am.* **105,** 3050–3067.

Somerville, P., K. Irikura, R. Graves, S. Sawada, D. Wald, N. Abrahamson, Y. Iwasaki, T. Kagawa, N. Smith, and A. Kowada (1999). Characterizing crustal earthquake slip models for the prediction of strong ground motion, *Seismol. Res. Lett.* **70,** 59–80.

Tinti, E., E. Fukuyama, A. Piatanesi, and M. Cocco (2005). A kinematic source-time function compatible with earthquake dynamics, *Bull. Seismol. Soc. Am.* **95,** 1211–1223.

Wells, D. L., and K. J. Coppersmith (1994). New empirical relationships among magnitude, rupture length, rupture width, rupture area, and surface displacement, *Bull. Seismol. Soc. Am.* **84,** 974–1002.

Yoshida, Y., H. Ueno, D. Muto, and S. Aoki (2011). Source process of the 2011 off the Pacific coast of Tohoku earthquake with the combination of teleseismic and strong motion data, *Earth Planets Space* **63,** 565–569.

Zhu, C., C. Wang, X. Shan, G. Zhang, Q. Li, J. Zhu, B. Zhang, and P. Liu (2022). Rupture models of the 2016 central Italy earthquake sequence from joint inversion of strong-motion and InSAR datasets: Implications for fault behavior, *Remote Sens.* **14,** 1819, doi: 10.3390/rs14081819.